Dye⋯TiO$_2$ Interfacial Structure of Dye-Sensitised Solar Cell Working Electrodes Buried under a Solution of I$^-$/I$_3^-$ Redox Electrolyte

Jonathan McCree-Grey[†,‡], Jacqueline M. Cole*[†,#,§,+], Stephen A. Holt[‡], Peter J. Evans[‡], Yun Gong[†]

[†]*Cavendish Laboratory, Department of Physics, University of Cambridge, J. J. Thomson Avenue, Cambridge, CB3 0HE. UK.*

[‡]*Australian Centre for Neutron Scattering, Australian Nuclear Science and Technology Organisation, Lucas Heights, New South Wales, 2234, Australia*

[#]*ISIS Neutron and Muon Source, STFC Rutherford Appleton Laboratory, Harwell Science and Innovation Campus, Didcot, Oxfordshire, OX11 0QX. UK*

[§]*Argonne National Laboratory, 9700 South Cass Avenue, Argonne, IL 60439, USA*

[+]*Department of Chemical Engineering and Biotechnology, University of Cambridge, West Cambridge Site, Philippa Fawcett Drive, Cambridge, CB3 0FS. UK*

Author for correspondence (J. M. Cole): jmc61@cam.ac.uk

1

Abstract

Dye-sensitised solar cells (DSCs) have niche prospects for electricity-generating windows that could equip buildings for energy-sustainable future cities. However, this 'smart window' technology is being held back by a lack of understanding in how the dye interacts with its device environment at the molecular level. A better appreciation of the dye$\cdots$TiO$_2$ interfacial structure of the DSC working electrodes would be particularly valuable since associated structure-function relationships could be established; these rules would provide a 'toolkit' for the molecular engineering of more suitable DSC dyes via rational design. Previous materials characterisation efforts have been limited to determining this interfacial structure within an environment exposed to air or situated in a solvent medium. This study is the first to reveal the structure of this buried interface within the functional device environment, and represents the first application of *in situ* neutron reflectometry to DSC research. By incorporating the electrolyte into the structural model of this buried interface, we reveal how lithium cations from the electrolyte constituents influence the dye$\cdots$TiO$_2$ binding configuration of an organic sensitiser, **MK-44**, via Li$^+$ complexation to the cyanoacrylate group. This dye is the molecular congener of the high-performance **MK-2** DSC dye, whose hexa-alkyl chains appear to stabilise it from Li$^+$ complexation. Our *in situ* neutron reflectometry findings are built up from auxiliary structural models derived from *ex situ* X-ray reflectometry and corroborated via density functional theory and UV/vis absorption spectroscopy. Significant differences between the *in situ* and *ex situ* dye$\cdots$TiO$_2$ interfacial structures are found, highlighting the need to characterise the molecular structure of DSC working electrodes while in their fully assembled device.

Keywords: *In situ* Neutron Reflectometry, dye$\cdots$TiO$_2$ buried Interface, Dye-Sensitised Solar Cell, Electrolyte Solution, *Ex situ* X-ray reflectometry

1 Introduction

Since the seminal demonstration of dye-sensitised solar cells (DSCs),[1] these devices have become a topic of increasing research interest, owing to their potential for low-cost, efficient and environmentally-friendly electrical power generation.[2] Indeed, these factors, coupled with the transparent nature of DSCs and their ability to perform particularly well under diffuse light conditions, imbues this technology with niche prospects for 'smart window' applications.[3-5] A typical DSC employs a photosensitive dye as the light harvester. This dye is adsorbed onto the surface of a TiO_2 nanostructure, such that the photoabsorbed dye can inject an electron into the TiO_2 conduction band; the dye$\cdots TiO_2$ composite thus acts as the working electrode of a DSC device. The electrical current passes to a counter electrode, composed of a transparent conducting oxide, which is classically coated by platinum to catalyse an electrolytic process whereby a liquid redox electrolyte (eg. I^-/I_3^-), that is sandwiched between the two electrodes, returns the photo-excited dye to its ground state, thereby completing the electrical circuit.[6]

To date, many different dye species have been synthesised and their power-conversion efficiency (PCE) examined in functional devices.[7] Historically, dyes based on metal-centred complexes, such as ruthenium[8-9] or zinc,[10] have achieved the highest efficiencies; with a zinc porphyrin-based dye topping 13.0% efficiency,[11] while another can reach 13.1% if co-sensitised with an organic chromophore.[12] However, increasingly restrictive environmental regulations stand against the use of metals in these dyes; and some, such as ruthenium, are also scarce in natural abundance. These factors make such dyes expensive to produce and unsuitable for cost-effective, environmentally friendly photovoltaic technologies.

Metal-free organic dyes have recently superseded the maximum PCE of DSCs containing metal-based dyes, via the record-breaking efficiency of 14.3% being obtained using a DSC working electrode that features two co-sensitised metal-free organic dyes.[13] A handful of

singly-sensitised organic dyes have also been able to challenge the historical DSC efficiencies set by singly-sensitised metal-complex dyes.[14-15] The development of metal-free organic-dyes is therefore taking the forefront of DSC research. Such developments are particularly compelling in view of the fact that metal-free organic dyes promise cheaper, more environmentally friendly synthetic routes and greater molecular design flexibility than their metal-containing counterparts.[7]

The dye is a particularly important constituent of a DSC device given it has a dual function, acting as the light harvester; and being responsible for the electron injection process that supplies the conduction band of the TiO_2 semiconductor to which the dye is adsorbed, to initiate the electrical circuit of a DSC. It is also commonplace to introduce alkyl chains into dye structures, to tune the corresponding dye$\cdots TiO_2$ interface against undesirable electron recombination or dye aggregation effects.[7,16-19] Given that these electronic and molecular characteristics define the key functions of the dye$\cdots TiO_2$ working electrode, [20-23] DSC performance is predicated on the nature of the structure, orientation and packing density of the dye at the TiO_2 interface.

A range of materials characterisation techniques have been used to infer these dye structural attributes at the TiO_2 interface. Such studies have generally been limited to *ex situ* methods,[24] wherein average dye orientations on exposed TiO_2 surfaces have been deduced via X-ray reflectometry[25-26] or near-edge X-ray absorption spectroscopy (NEXAFS).[27, 28] A few pseudo *in situ* infra-red spectroscopy[29] or atomic force microscopy[30] studies on dye$\cdots TiO_2$ composites (pseudo *in situ* in the sense that the composites reside within device-relevant solvents) have nonetheless inferred average dye orientations on TiO_2 with help from theoretical calculations; while a similarly pseudo *in situ* NEXAFS[31] study draws qualitative conclusions about dye orientation in solvents with the aid of corroboratory findings from photoelectron spectroscopy. Meanwhile, two recent *ex situ* scanning tunnelling microscopy (STM) studies[32-33] have

4

experimentally imaged the anionic ruthenium-based dye, N3, residing on TiO_2 surfaces. One of these studies[33] also employed scanning tunnelling spectroscopy (STS)[33] which distinguished various conformations of N3 dye anions existing on TiO_2. The imaging part of this study was able to distinguish dye monomers from its dimers, but not molecular features at the resolution needed to discern dye structure, orientations or packing densities on TiO_2 surfaces. One therefore needs a way to probe this dye$\cdots TiO_2$ interfacial structure at the atomic scale, and within a more closely emulated device environment, in order to complement these state-of-the-art developments in materials characterisation.

This work will show that the complementary use of X-ray and neutron reflectometry presents a way forward in this regard. To this end, we employ *in situ* neutron reflectometry to probe the buried interfacial structure of a DSC working electrode within a solid-liquid environment, and support our results with *ex situ* XRR measurements, density functional theory calculations and UV/vis absorption spectroscopy. To the best of our knowledge, this is the first report of a study where neutron reflectometry has been employed in DSC research. Moreover, the study is unprecedented in demonstrating how a materials characterisation tool can access this dye$\cdots TiO_2$ structure while it is embedded within a buried interface and submerged by a redox (I^-/I_3^-) electrolyte solution, i.e. within a material environment that emulates a functional DSC device.

The subject materials for these reflectometry studies comprise thin films of TiO_2 sensitised with one of two metal-free organic dyes and submerged within an electrolyte solution to create a solid-liquid interface. The high performance dye, 2-cyano-3-[5‴-(9-ethyl-9H-carbazol-3-yl)-3′,3″,3‴,4-tetra-n-hexyl-[2,2′,5′,2″,5″,2‴]-quater thiophen-5-yl]acrylic acid (**MK-2**),[34] and its smaller analogue, 2-cyano-3-(5-(9-ethyl-9H-carbazol-3-yl)thiophen-2-yl)acrylic acid (**MK-44**), as shown in **Figure 1**, were the two selected sensitisers. This choice reflects the wide interest that the MK series of metal-free organic dyes has attracted on account of their large

molar adsorption coefficients,[22] good long-term stability[35] and high-performance,[14] with **MK-2** achieving one of the highest efficiencies for a metal-free organic dye of nearly 8%.[34] In addition, DSCs that employ **MK-2** have recently demonstrated success in their application as electricity-generating windows.[36]
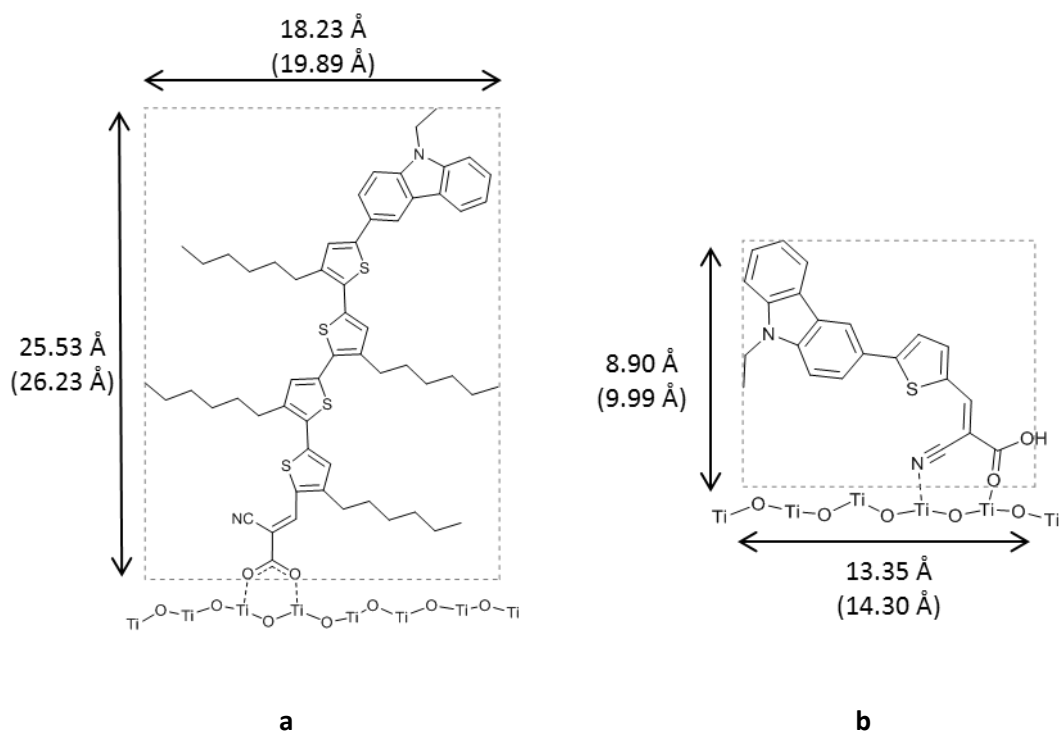

Figure 1 Molecular structures and preferred TiO_2 binding modes of; a) **MK-2**; and b) **MK-44**.[37,38] Annotated lateral molecular lengths and widths are taken from their crystal structures which were derived from X-ray diffraction data.[39] Since neutrons are able to detect hydrogen atoms much better than X-rays, additional values (in parentheses) for these lateral dimensions are presented which incorporates the explicit position and bond lengths of hydrogen atoms, whose presence may be discounted during XRR studies. It is notable here, that the hydrogen of the carboxylic acid hydroxyl group on **MK-44** is not considered during these measurements, as when bound to the TiO_2 surface, this hydrogen is only present via a hydrogen bond to the exposed TiO_2 surface hydroxide groups. For reference, an average carbon-hydrogen bond length is considered to be 1.08 Å.[40]

2 Experimental and Computational Methods

2.1 Preparation and Sensitisation of TiO_2 Thin-films

In accordance with previous work,[25] amorphous TiO_2 thin films were deposited on silicon (100) wafers in order to provide the atomically flat surface required for reflectometry measurements. This practical requirement for TiO_2 can be met while retaining device-relevant results: previous work has shown that organic molecules adsorb onto TiO_2 with the same type of binding mode, whether they are sensitised onto amorphous or crystalline TiO_2.[41,42] These thin films were produced using an ASM Microchemistry flow-type, hot-walled, F-120 atomic layer deposition (ALD) reactor, which was maintained at 1 mBar pressure and using a deposition temperature of 120 °C. Vaporous $TiCl_4$ and H_2O precursors were delivered from Peltier-cooled reservoirs maintained at 20 °C, following a sequential dosing scheme of 0.4 s $TiCl_4$ exposure, a 1.0 s N_2 purge, a 1.0 s H_2O pulse and a final 1.5 s N_2 purge.[43] This process was repeated for 200 cycles. A TiO_2 growth rate of ~0.04 nm/cycle yielded a ~8 nm thick TiO_2 thin film. The surface appearance of this film was imaged via atomic force microscopy and its amorphous nature was confirmed by Bragg-Brentano X-ray diffraction measurements (see Electronic Supplementary Information, §1).

Prior to dye sensitisation, these films were heated to 80 °C for a minimum of 30 minutes in order to remove any residual water on their surface. Successful water eradication was confirmed by performing X-ray reflectometry (§see 2.2) on the untreated substrate; whereupon the fits to the data required only a two-layer model, thus confirming the absence of any surface contamination such as residual trace amounts of water. Sensitisation was achieved by submersing the TiO_2 films in a 0.3 mM dye solution of **MK-2** (95%, Sigma-Aldrich) or **MK-44** (synthesised via the method of Koumura et al[34]) in 1:1:1 acetonitrile:*tert*-butanol:toluene

for 20 hours. The resulting films were rinsed with neat acetonitrile and dried under a flow of nitrogen gas prior to being subject to reflectometry measurements.

2.2 X-ray Reflectometry (XRR)

XRR measurements were conducted using a Panalytical X'pert Pro reflectometer that employed a Cu Kα X-ray source (λ = 1.541 Å). The X-ray beam was collimated using a Göbel mirror with a 0.1 mm slit and a post-sample parallel collimator. Reflectivity data were collected over a detector range of $0.1° < 2\theta < 10.0°$, incrementing in 0.02° steps, with a count time of 10 s per step. Data were acquired for the TiO_2 substrate before and after its dye sensitisation, using the same substrate. The results were refined using the MOTOFIT package[44] for Igor Pro (Wavemetrics) to reveal associated structural parameters, with X-ray reflectivity plotted as a function of the momentum transfer vector (Q) perpendicular to the TiO_2 surface (1).

$$Q = 4\pi \left(\frac{\sin(\theta)}{\lambda} \right) \tag{1}$$

Nominal values for the X-ray scattering-length density (SLD_x) for each layer were used to prepare initial structural models, using a three-layer approach, whereby values of 20.1×10^{-6} $Å^{-2}$, 18.9×10^{-6} $Å^{-2}$ and 31.2×10^{-6} $Å^{-2}$ represented the silicon wafer, the native oxide layer and TiO_2 film, respectively. SLD_x values of 11.2×10^{-6} $Å^{-2}$ and 12.7×10^{-6} $Å^{-2}$ were calculated for **MK-2** and **MK-44** respectively, using (2):

$$SLD_x = \frac{r_e Z}{V} \tag{2}$$

where r_e refers to the classical electron radius (2.81×10^{-15} m), Z is the sum of atomic numbers (*ie*. the total number of electrons) in each molecule (512 and 194 for **MK-2** and **MK-44** respectively), and V is the molecular volume of the dye, determined from its crystal structure (1284.34 $Å^3$ and 428.96 $Å^3$ respectively).[39]

2.3 Neutron Reflectometry (NR)

Three electrolyte solutions were prepared and sequentially tested with the sensitised TiO_2 substrate in a solid-liquid cell: neat deuterated acetonitrile (d_3-MeCN, 99.8%, Sigma-Aldrich); 0.7 M LiI (99.99%, Sigma-Aldrich) in d_3-MeCN; and 0.7 M LiI & 0.05 M I_2 (99.8%, Sigma-Aldrich) in d_3-MeCN. For simplicity, these are henceforth referred to as solutions 1, 2 and 3, respectively.

Neutron reflectometry measurements were conducted using the Platypus time-of-flight reflectometer at the OPAL research reactor, ANSTO, Sydney, Australia.[45] All measurements followed the same scan parameters using a cold neutron spectrum of 3.0 Å $< \lambda <$ 18.0 Å, with a resolution $\Delta Q/Q$ = 5.1 %. Beam profiles were collected at θ = 0.5°, 2.0° and 4° giving maximum Q range of 0.006 – 0.300 Å^{-1}. Three measurements were conducted on each dye using solutions 1-3; for solutions 2 and 3, neutron data acquisition was initiated 10 minutes after LiI or I_2 had been added in order to ensure sufficient time for solution mixing and chemical reactions. Data were reduced taking into account direct beam transmission through the silicon substrate and corrected for background.

The reduced data were co-refined using the MOTOFIT package[44] for Igor Pro (Wavemetrics) with Monte-Carlo re-sampling[46] to reveal associated structural parameters and corresponding standard deviations, with reflectivity plotted as a function of the momentum transfer vector (Q) perpendicular to the TiO_2 surface (**1**). Further details on this fitting process are provided in the Electronic Supplementary Information, §3 and §6.

Nominal values for the neutron scattering-length density (SLD_n) for each layer (**Table 1**) were calculated using (**3**) and used to prepare initial structural models.

$$SLD_n = \frac{\sum b_c}{V} = \frac{N_A \rho \sum b_c}{M} \qquad (3)$$

where $\sum b_c$ is the sum of isotopic coherent scattering lengths in the molecule;[47] N_A is Avogadro's constant; ρ the mass density; V the molecular volume of the dye, determined from its crystal structure; and M is the molecular mass.

All of the NR fits were modelled using a three-layer approach, with a 5 Å native oxide layer ($SLD_n = 3.47 \times 10^{-6}$ Å^{-2}). The SLD_n of the silicon super-phase was fixed at 2.07×10^{-6} Å^{-2} and the TiO_2 substrate at 2.10×10^{-6} Å^{-2} after initial model fitting. Since the length-scale of these dyes was on the limits of detection for these NR data, the interfacial layer roughness values were fixed in accordance with XRR results, with R = 2.5 Å, 2.5 Å and 3.5 Å for the silicon super-phase, native oxide and TiO_2 interfaces, respectively (**Table 1**).

Table 1 Calculated SLD_n values for the materials of interest

	Material	**Chemical Formula**	**Mass Density /g cm^{-3}**	**Molecular Volume /Å^3**	**Neutron SLD$_n$ (10^{-6}) /Å^{-2}**
Electrolyte	*d$_3$- MeCN*	C_2D_3N	0.872	-	4.90
	I$_2$	I_2	4.93	-	1.24
	LiI	LiI	4.08	-	0.62
Dye	**MK-2**	$C_{58}H_{70}N_2O_2S_4$	-	1284.34 [39]	1.29
	MK-44	$C_{22}H_{16}N_2O_2S$	-	437.1 [39]	2.74
Substrate	*TiO$_2$*	TiO_2	3.70[48]	-	2.28
	Native Oxide	SiO_2	2.20	-	3.47
	Silicon	Si	2.33	-	2.07

Reflectivity models were constructed and fitted to achieve the best least-squares fits. Models were constructed initially using two layers (SiO_2 and TiO_2) with a silicon super-phase. A third, dye-layer was subsequently added to yield the simplest yet most physically reasonable model. The results presented here arise from the best fits to the data using these simple 3-layer models, applying physically reasonable values. It should be noted that when fits were attempted with

model parameters completely unconstrained, the dye-layer thicknesses were greater than those calculated as the maximum possible thicknesses for a dye monolayer. As a result, it was necessary to constrain the dye thickness to a sensible range of values. Establishing such boundary conditions for the model ensured physically reasonable results were realised, based on known dimensions and scattering length densities of constituent molecules. Although this made fitting more difficult, consistent fits were achieved via a combination of co-refinement of similar data sets and Monte-Carlo re-sampling (see Electronic Supplementary Information for details, §5).

2.4 UV/vis absorption spectroscopy

A single layer mesoporous TiO_2 thin-film was prepared on a microscope slide by the doctor blade technique. This was then sensitised in a 0.3 mM solution of **MK-44** dye in 1:1:1 acetonitrile:*tert*-butanol:toluene solvent for 5 minutes, before being subsequently rinsed with neat acetonitrile. The film was then treated with a 0.5 M solution of lithium iodide (99.9 %, Sigma-Aldrich) in acetonitrile (anhydrous, Sigma-Aldrich), added via a pipette with a 5 s rinse, before being further rinsed with minimal amounts of neat acetonitrile. The absorption spectrum of the film was measured prior to and post lithium iodide treatment using a Cary 300 UV/vis Spectrophotometer (Agilent Technologies). Further details are given in the Electronic Supplementary Information, §6.

2.5 Density functional theory calculations

Electronic structure calculations of the dye$\cdots TiO_2$ interface were performed using density functional theory within the Gaussian09 software.[49] A nine-unit TiO_2 cluster[50-51] was used to form a dye$\cdots TiO_2$ adsorption model. The structure and energy of the bidentate bridging and CN/COO adsorption modes[24] were calculated with and without surrounding Li^+ ions, respectively (See Electronic Supplementary Information, §6). Geometry optimisations were

carried out via the hybrid functional B3LYP[52] coupled with the 3-21g* basis set. Frequency calculations were conducted in order to confirm the optimised geometry possessed a minimum energy at same theory level.

3 Results and Discussion

The ultimate goal of this work is to study the dye···TiO_2 structure at a buried interface, i.e. under the environmental conditions which correspond to the DSC working electrode within a functional device. Within this scope, the structure, orientation and packing density of the dye at the TiO_2 interface are sought. Reflectometry stands to be helpful since it can deliver such structural information via the measurement of dye···TiO_2 layer thickness, density, and interfacial roughness.[25,26] More specifically, neutron reflectometry (NR) is ideally suited to such a study, since the small size of a neutron and its zero charge gives it the ability to penetrate deep into a material. In addition, NR is generally able to distinguish interfacial layers from each other with good contrast, since neutron scattering length density (SLD_n), which defines this contrast, tends to be distinct for a given layer. Such distinction results from the complicated nature of neutron-nuclei interactions in neutron scattering.

To this end, the appropriate sample environment for such a study would comprise a solid-liquid environment of a DSC working electrode, wherein the dye-sensitised TiO_2 solid is submerged by a redox electrolyte (I^-/I_3^-) solution; thus, emulating the DSC working electrode within a functional device. However, since there appears to be no previous report of any DSC-based neutron reflectometry, let alone an *in situ* DSC-based neutron reflectometry study, it seemed logical to build up to this study by prefacing it with initial experiments on exposed DSC working electrodes using *ex situ* X-ray reflectometry (XRR). Therein, XRR has already demonstrated its use in the study of dye···TiO_2 interfacial structures, and linking such structure with device performance.[25] Accordingly, XRR studies can provide baseline interfacial structure

details about the subject dyes on the TiO_2 surface in a solid-air environment, prior to embedding the DSC working electrode within the electrolyte solution for the more complicated, and unprecedented, *in situ* neutron reflectometry investigations.

3.1 Dye···TiO₂ Interfacial Structure of Exposed DSC Working Electrodes

TiO_2 films sensitised with **MK-2** or **MK-44** dye were first measured in a solid-air environment using *ex situ* XRR, to provide reference structural details about the exposed DSC working electrode for the subsequent *in situ* NR study. Each sensitised substrate was measured four times, at different points about the sample surface. Representative plots of experimentally observed and fitted data for **MK-2** (red) and **MK-44** (blue) adsorbed onto the amorphous TiO_2 substrate are shown in **Figure 2** (data sets showing all four measurements for each dye, and their SLD_x profiles, can be found in the Electronic Supplementary Information, §2.2). Structural parameters (SLD_x; thickness; and roughness) for both the dye-layer and TiO_2 substrate (**Table 2**) were obtained from refinements of a three-layer model, consisting of: dye-layer; TiO_2 film; and a 5 Å thick native oxide layer on a silicon sub-phase. The SLD_x of the native oxide layer and silicon substrate were fixed at 18.9×10^{-6} Å^{-2} and 20.1×10^{-6} Å^{-2} respectively.
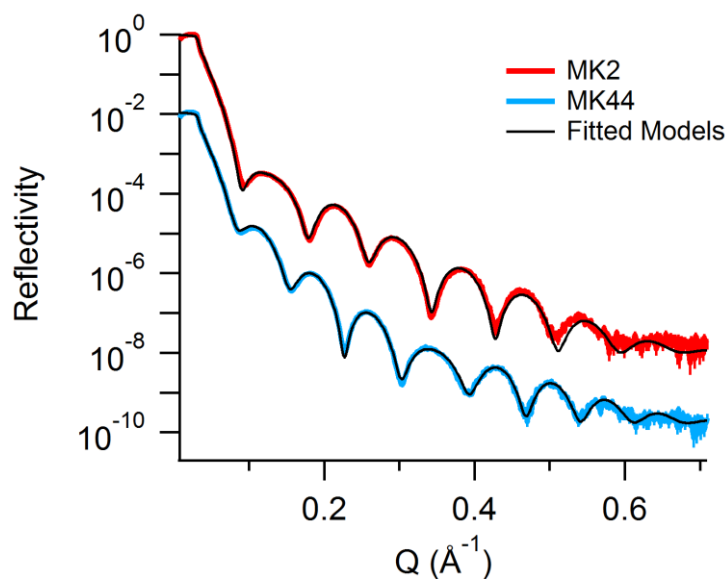
Figure 2 Representative X-ray reflectivity profiles for TiO_2 thin-film sensitised by **MK-2** (red) and **MK-44** (blue) dyes. The corresponding fitted and refined structural models are shown in black. The **MK-44** (blue) trace has been offset by a factor of 10^{-2} for clarity.

Table 2 Structural parameters as determined by XRR for **MK-2** and **MK-44**, along with their respective TiO_2 substrates.

		MK-2	**MK-44**
Dye layer	Dye Formula	$C_{58}H_{70}N_2O_2S_4$	$C_{22}H_{16}N_2O_2S$
	Thickness / Å	23.2 ± 0.2	9.6 ± 0.2
	SLD_x ($\times 10^{-6}$) / Å^{-2}	10.1 ± 0.4	9.6 ± 0.3
	Surface roughness / Å	6.4 ± 0.2	3.6 ± 0.1
	Mass density /g cm^{-3}	1.11	1.09
TiO$_2$ layer	Thickness / Å	73.8 ± 0.6	82.5 ± 0.5
	SLD_x($\times 10^{-6}$) / Å^{-2}	30.6 ± 0.2	30.5 ± 0.5
	Interfacial roughness / Å	3.6 ± 0.3	4.2 ± 0.1

3.1.1 MK-2 Dye

3.1.1.1 Dye orientation on the TiO₂ surface. Computational results have shown that the **MK-2** dye binds to the TiO_2 surface via a carboxylate bidentate bridging mode.[37] For modelling

purposes, the associated dye$\cdots$TiO$_2$ separation is taken as the average COO$^-\cdots$TiO$_2$ bond length (2.05 Å).[29] These reference structural parameters indicate that the maximum possible dye layer thickness (d_{max}) for a monolayer of **MK-2** is 27.58 Å, c.f. the sum of the dye$\cdots$TiO$_2$ separation, plus the fully extended length of the dye molecule, defined as the distance between atoms O2 and C52 in the crystal structure (25.53 Å; see Electronic Supplementary Information, §2.1).[39] A dye layer thickness of d_{max} would therefore correspond to the situation where all dye molecules align perpendicular to the TiO$_2$ surface.

The XRR results reveal an actual dye-layer thickness (d_{obs}) of 23.2 ± 0.2 Å, indicating that **MK-2** is adsorbed as a monolayer adopting a tilt angle (α) of 65.1 ± 1.1° with respect to the TiO$_2$ surface plane **(Figure 3).** The standard deviation for the tilt angle is presented as the error in the measured dye-layer thickness over the four XRR measurements.
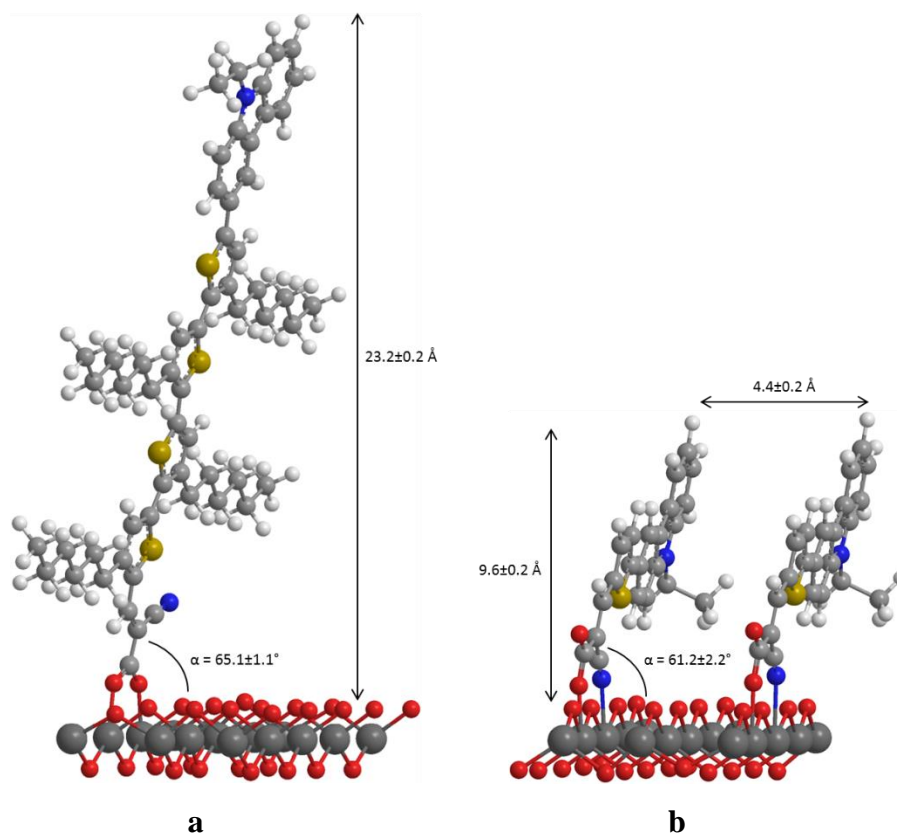

| a | b |

Figure 3 Visualisation of a) **MK-2**; and b) **MK-44** bound to a TiO$_2$ surface (note that potential hydrogen bonding between the carbonyl group and exposed hydrogens of the TiO$_2$ surface are

emitted for clarity).[34] Models were created using ChemBio3D (Perkin Elmer). The dye⋯TiO$_2$ separation was fixed at 2.05Å and the molecular tilt adjusted to achieve a layer thickness representative of that observed by XRR. The tilt angle (α) of the dye bound to the TiO$_2$ surface is calculated from d$_{max}$ and d$_{obs}$ values using basic trigonometric considerations (as shown in previous work and Electronic Supplementary Information, §2.3);[25] the theoretical area-per-molecule (APM) of the dye, as projected onto the TiO$_2$ surface, is calculated by multiplying the molecular width of the dye with its length (L) as projected on the TiO$_2$ surface, L = d$_{max}$cos(α). This calculation assumes a planar dye molecule which is reasonable in the case of the **MK-2** and **MK-44** dyes, given their crystal structures show exceptional levels of molecular planarity.[39]

3.1.1.2 Dye coverage over the TiO$_2$ surface. An SLD$_x$ of 10.1×10^{-6} Å^{-2} was observed for the **MK-2** dye, corresponding to a dye-layer with mass density of 1.11 g cm^{-3} (**Equation 4**), comparable to other high performance dyes.[26]

$$SLD = \frac{r_e N_A \rho Z}{M} \qquad \textbf{(4)}$$

where N_A is Avogadro's number, ρ is the mass density and M is the molecular mass of **MK-2** (955.42 u). The average measured area per molecule (APM) as projected onto the TiO$_2$ surface (61.6 ± 1.0 Å^2) was determined from this SLD value, according to **Equation 5**:

$$APM = \frac{r_e Z}{d_{obs}(SLD)} \qquad \textbf{(5)}$$

where d_{obs} is the observed dye-layer thickness.

$$[dye]_{surf} = \frac{1}{N_A \times APM} \qquad \textbf{(6)}$$

The associated dye surface concentration, 2.7×10^{-10} mol cm^{-2} ((**6**), is of a magnitude expected for a dye monolayer and is in good agreement with such concentrations measured in previous

dye absorption studies on amorphous TiO_2 films.[25, 53] **Equation (7** determines a dye volume fraction (φ) of 0.90 ± 0.02 upon the TiO_2 surface, similar to values obtained in literature.[18]

$$\varphi = \frac{SLD_{obs}}{SLD_{calc}} \qquad (7)$$

where SLD_{obs} is the observed scattering length density for the dye-layer, and SLD_{calc} is the scattering length density calculated using **Equation 2** which assumes 100% surface coverage.

The maximum possible width of the **MK-2** dye molecule is 18.23 Å, as defined by the separation between the C49 and C59 atoms in its crystal structure, whose vector lies perpendicular to the longest molecular axis (see Electronic Supplementary Information, §2.1).[39] The calculated APM for a single molecule is therefore given as 211.7 Å^2 (**Figure 3**). This effectively represents the maximum theoretical molecular footprint of the dye as per its projection onto the TiO_2 surface.

3.1.1.3. Intermolecular spacing between dyes on the TiO_2 surface. In previous work, it has been possible to estimate inter-dye spacing on the TiO_2 surface via a measure of the intermolecular separation between parallel molecular planes of dyes.[25] However, the literature suggests that the hexa-alkyl chains of adjacent **MK-2** molecules intertwine significantly,[14, 54] the level of which is not directly determinable using XRR. Indeed, the fact that the theoretical molecular footprint of a single, isolated, **MK-2** molecule is ~3.5 times larger than that measured for those on the TiO_2 surface, is suggestive of such intertwining occurring in this instance. The crystal structure of **MK-2** shows adjacent molecules with up to five hexa-alkyl chain carbons intertwining (equating to a distance of up to ~5.05 Å along each intertwining chain).[39] Such an inter-digitation of alkyl groups would reduce the effective width of the **MK-2** molecule on the TiO_2 surface to ~8.13 Å. Given the measured APM of 61.6 ± 1.0 Å^2 and tilt angle of $\alpha = 65.1 \pm 1.1°$ for **MK-2** on TiO_2, as determined by XRR at the given dye coverage, the intermolecular

separation of **MK-2** on the TiO$_2$ surface will therefore be interdependent upon this chain inter-digitation. It is therefore deemed more appropriate to suggest a range of expected intermolecular separation, 3.26 Å – 7.01 Å, dependent upon the extent of hexa-alkyl chain inter-digitation (see Electronic Supplementary Information, §2.4) at the given dye coverage. It would also not seem unreasonable to postulate that molecules experiencing varying degrees of hexa-alkyl chain inter-digitation, and therefore intermolecular separation, may co-exist on the same surface.[54]

3.1.2   MK-44 Dye

3.1.2.1 Dye orientation on the TiO$_2$ surface. Zhang et al have shown that small cyanoacrylic-bound dyes (similar in structure to **MK-44**) energetically prefer a binding mode which employs both the carboxylic acid and cyanide group of the cyanoacrylic acid moiety (**Figure 1 (b)**), over the bidentate bridging mode that is preferred for **MK-2**.[38] They report a CN$\cdots$TiO$_2$ separation of 2.20 Å for this so-called CN/COO binding configuration.[38] Steric hindrance associated with the hexa-alkyl chains in **MK-2** appears to preclude the dye$\cdots$TiO$_2$ binding configuration indicated for **MK-44**, judging from its crystal structure[39]. A molecular width of 13.35 Å was calculated for **MK-44**, as defined by the separation between O1 and C1 atoms in its crystal structure (see Electronic Supplementary Information, §2.1).[39] **MK-44** molecules may extend up from the TiO$_2$ surface to a maximum, d_{max}, of 10.95 Å, as determined by the sum of the COOH$\cdots$TiO$_2$ separation (2.05 Å)[29] and the molecular height of **MK-44** which is defined as the distance between C3 and O2 atoms (see Electronic Supplementary Information, §2.1) where the dye molecule would align perpendicular to the TiO$_2$ surface (8.90 Å).[39]

The XRR results on **MK-44** reveal a dye-layer thickness of 9.6 ± 0.2 Å. Based on the model structural parameters defined above, this suggests that a monolayer of **MK-44** dye molecules exists, wherein the dye adopts an average tilt angle (α) of 61.2 ± 2.2° relative to the TiO$_2$ surface (**Figure 3**). This is indicative of the suggested binding geometry.

3.1.2.2 Dye coverage over the TiO$_2$ surface. The SLD_x for the **MK-44** dye-layer in the XRR structural model is $9.6 \pm 0.2 \times 10^{-6}$ Å^{-2}, which corresponds to a dye-layer with density of 1.09 g cm^{-3} (**Equation 4**), very similar to that observed for **MK-2**. The average measured area per molecule (APM) as projected onto the TiO$_2$ surface (59.3 ± 2.3 Å^2) was duly calculated from **Equation 5**, and is comparable to a theoretical APM of 70.2 Å^2. A dye surface concentration of 2.8×10^{-10} mol cm^{-2} was determined via **Equation 6**, again comparable to that of **MK-2**. The ratio of observed and calculated SLD values (**Equation 7**) yielded an **MK-44** volume fraction (φ) of 0.75 ± 0.02 on the TiO$_2$ surface. All of these factors indicate that a similar level of dye coverage was achieved for the **MK-2** and **MK-44** sensitized TiO$_2$ samples used in these XRR experiments.

3.1.2.3. Intermolecular spacing between dyes on the TiO$_2$ surface. The average inter-dye spacing on the TiO$_2$ surface, as defined by the distance between parallel molecular faces in adjacent dyes, was estimated to be 4.4 ± 0.2 Å assuming no lateral overlap (**Figure 3 (b)**). This value lies outside the generally accepted range of distances for $\pi \cdots \pi$ stacking interactions (< 3.3-3.8 Å).[55] The presence of such interactions may have otherwise been assumed intuitively to be occurring between **MK-44** molecules on the TiO$_2$ surface, due to the small size and largely delocalised π-electronic structure of this dye. This value is nonetheless smaller than the theoretical 5.3 Å molecular length, as projected onto the surface, for an isolated **MK-44** molecule, suggesting a minimal intermolecular facial overlap of 0.9 Å.

3.2   Dye$\cdots$TiO$_2$ Interfacial Structure of DSC Working Electrodes Buried under a Solution of I$^-$/I$_3^-$ Redox Electrolyte

Having obtained this reference structural information on the exposed MK dye$\cdots$TiO$_2$ interfaces via XRR, these interfacial structures were then probed within the functional DSC device environment using *in situ* neutron reflectometry. A solid-liquid sample environment, which

emulated that of the working electrode within the functional DSC device, was created by submerging the dye···TiO_2 solid interface within a redox electrolyte (I^-/I_3^-) solution, which is bounded with FTO glass coated with a platinum catalyst. Each interface was tested under two different electrolyte solution conditions, one containing LiI in d_3-MeCN and the other hosting I_2 as well as LiI in d_3-MeCN. Each interface was also studied within a third solution that contained only d_3-MeCN solvent, for the purposes of comparison. A deuterated solvent was used in order to enhance the SLD_n contrast, and therefore the reflectometry signal of the dye-liquid interface. The calculated neutron SLD_n values for **MK-2** and **MK-44** are 1.3×10^{-6} Å^{-2} and 2.7×10^{-6} Å^{-2} (**(3)**, compared to 4.9×10^{-6} Å^{-2} and 1.3×10^{-6} Å^{-2} for the deuterated and hydrogenated isotopomers of acetonitrile, respectively. *In situ* neutron reflectometry was applied in transmission mode whereby neutrons penetrated through a silicon substrate to reach each solid-liquid sample environment, as illustrated in **Figure 4(a)**. The accompanying **Figure 4(b)** shows how the SLD_n variation of each layer of this emulated DSC device exhibits sufficient contrast for it to be used to discriminate NR signal exclusively from the desired dye···TiO_2 interfacial structure.

Figure 5 shows the experimentally observed and fitted NR data for the **MK-2** and **MK-44** sensitised TiO_2 films, in the presence of solutions 1 (d_3-MeCN, red); 2 (d_3-MeCN + LiI, orange); and 3 (d_3-MeCN + LiI + I_2, green) respectively. The effective dye layer contribution to the data is illustrated in Figure S9 of the Electronic Supplementary Information, §3.1. The corresponding refined structural parameters are presented in **Table 3**.
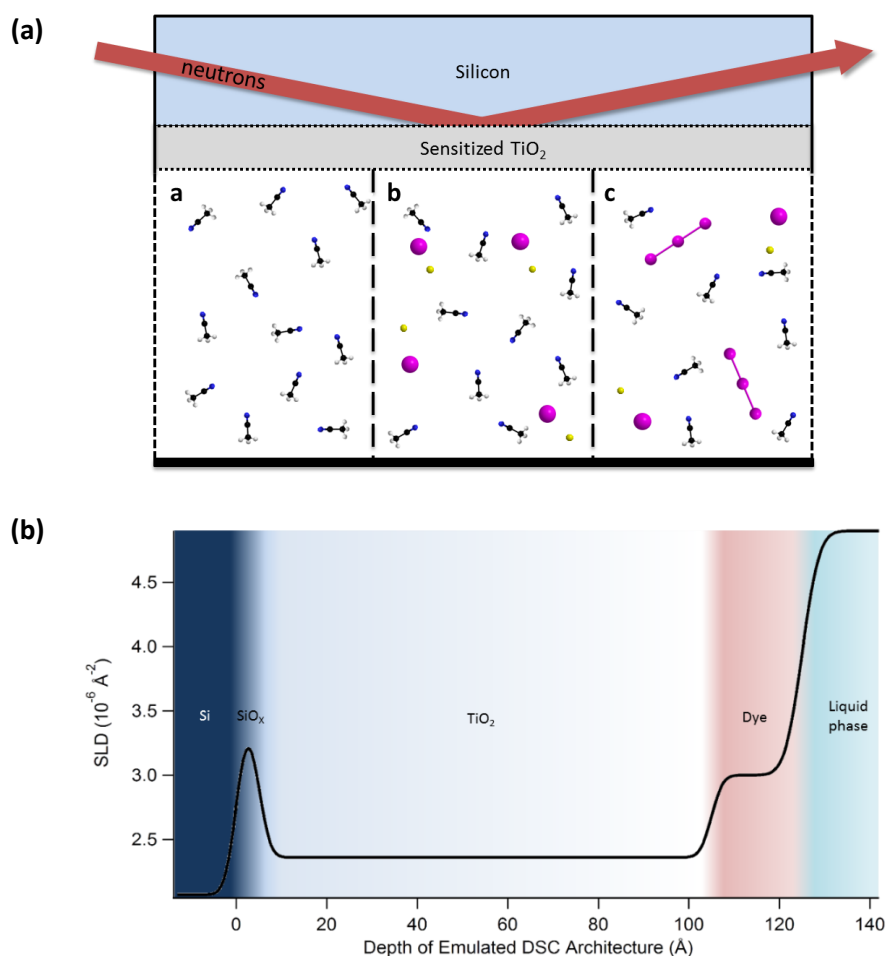
Figure 4*(a)* Schematic illustration of the dye sensitised TiO_2 sample within the solid-liquid environment. The three different solutions (1-3) are represented by sections a-c respectively, where a) is neat d_3-MeCN; b) is lithium (yellow) iodide (pink) in d_3-MeCN; and c) is the iodide:tri-iodide (pink, tri-atomic structure) in d_3-MeCN formed upon addition of I_2 to the previously stated LiI solution. These sections are displayed solely for the purposes of illustration; each solid-liquid interface was prepared and tested using individual solutions. The solution is bounded by FTO glass coated with a platinum catalyst. (b) SLD_n as a function of increasing depth of the emulated DSC device architecture, revealing the neutron scattering contrast variation that permits the exclusive determination of dye$\cdots$$TiO_2$ interfacial structure within its buried interface environment.
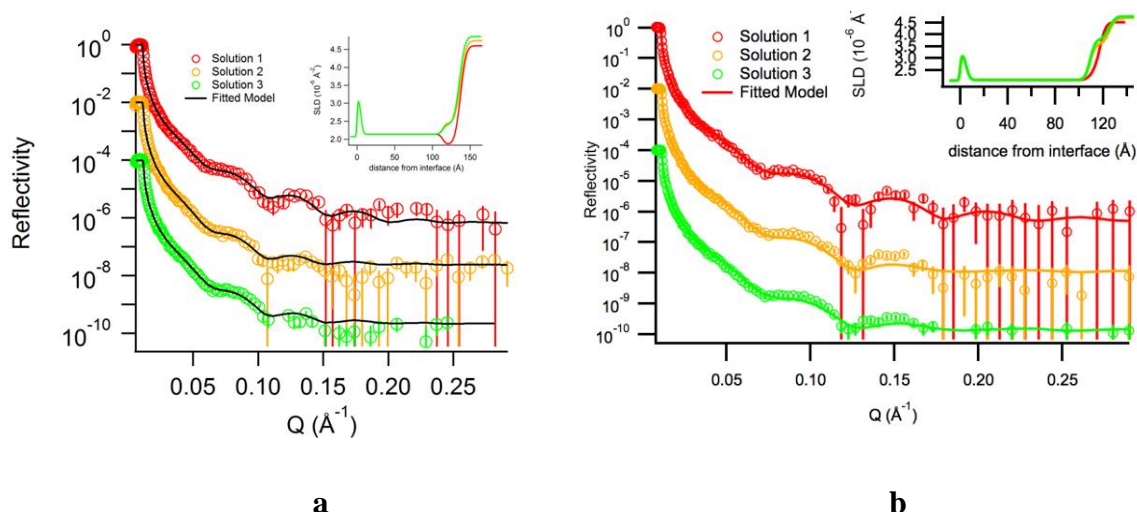
21

<div align="center">a   b</div>

Figure 5 Reflectivity profiles for (a) **MK-2** and (b) **MK-44** dyes sensitised on an amorphous TiO₂ thin-film and submerged within solution 1 (d₃-MeCN, red), 2 (d₃-MeCN + LiI, orange), or 3 (d₃-MeCN + LiI + I₂, green). The thin overlaid lines represent the co-refined models fitted to their corresponding datasets. Corresponding SLD_n profiles are presented as Figure insets.

Table 3 Structural parameters determined by NR for TiO₂ sensitised by **MK-2** or **MK-44** dyes, submerged by a solution 1 (d₃-MeCN), 2 (d₃-MeCN + LiI), or 3 (d₃-MeCN + LiI + I₂), and supported by a silicon substrate. Underlined values were fixed during the refinement procedure for the purposes of simplification and to minimise any model ambiguity. After initial model fitting, the solution SLD_n was fixed based on the position of the reflectivity critical edge, which is proportional to the SLD_n of the solution phase and defined as $Q_c = \sqrt{16.\pi.\Delta SLD}$. The SLD_n was shown to increase from solutions 1-3 (See Electronic Supplementary Information, §4)

		Dye Layer			**TiO₂ Layer**			**Solution**	
Dye	**Solution**	**t /Å**	**SLD_n (x10⁻⁶) /Å⁻²**	**R / Å**	**t /Å**	**SLD_n (x10⁻⁶) /Å⁻²**	**R / Å**	**SLD_n (x10⁻⁶) /Å⁻²**	**χ²**
MK-2	1	23.6±1.9	1.9±0.1	6.0	108.6±2.1	2.1	3.5	4.60	2.52
	2	23.8±1.9	2.5±0.1					4.74	2.31

MK-44								
	3	22.2±1.5	2.4±0.1				<u>4.86</u>	2.38
MK-44	1	9.2 ±0.7	2.9 ±0.6	4.0	107.6 ±2.3		<u>4.51</u>	1.61
	2	15.9 ±1.0	3.6 ±0.4				<u>4.67</u>	4.68
	3	15.9 ±1.0	3.8 ±0.4				<u>4.74</u>	3.02

These refined parameters were compared across the three solutions used, in order to assess the effect of the electrolyte medium on the **MK-2** or **MK-44** dye···TiO$_2$ interfacial structures. In the discussion that follows, XRR results are frequently used for reference, except where the d_{max} value is concerned. This parameter is re-defined for the NR study since the XRR data analysis ignored the hydrogen atoms present in the dye for the calculation of d_{max}, owing to their effective invisibility on account of the negligible X-ray scattering from hydrogen; while hydrogens produce significant neutron scattering and so will contribute towards the observed dye layer thickness. The d_{max} values for the NR study therefore included hydrogens explicitly in their calculation. To this end, the molecular length of **MK-2** was taken as the distance between O2 and H52 atoms along the molecular mean plane of its crystal structure (26.23 Å);[39] and its molecular width (20.44 Å) was defined as the distance between the H59 and H49 atoms, whose corresponding vector lies perpendicular to the molecular length (see Electronic Supplementary Information, §2.1). Accordingly, the maximum dye thickness of a monolayer of **MK-2** (d_{max}) was computed by summing this molecular length with the reference dye···TiO$_2$ binding separation (2.05 Å)[29], i.e. d_{max} for **MK-2** is 28.28 Å, when considering hydrogen atoms.

The d_{max} value of **MK-44** for NR data analysis (12.04 Å) was calculated in a similar fashion, arising from the sum of its molecular length of 9.99 Å, defined as the distance between atoms O2 and H3, plus the dye···TiO$_2$ separation (2.05 Å). The molecular width of **MK-44**, was also re-determined to incorporate hydrogen explicitly for the NR studies, using the separation

between atoms O1 and H1 (14.30 Å) to define the value. This width was employed in calculations that involve the molecular footprint of the dye as projected on to the TiO_2 surface, for a specified dye$\cdots TiO_2$ binding configuration (see Electronic Supplementary Information, §2.1).

3.2.1 Buried MK-2 dye$\cdots TiO_2$ solid interfaces

3.2.1.1 MK-2 dye$\cdots TiO_2$ solid interface submerged within an acetonitrile solution

NR results on the **MK-2** dye$\cdots TiO_2$ interface under neat d_3-MeCN (solution 1) reveal a dye layer thickness of 23.6 ± 1.9 Å with an SLD_n of $1.9 \pm 0.1 \times 10^{-6}$ Å^{-2}. The surface roughness was fixed at 6 Å, based on XRR data, in order to simplify the modelling process. This yields a dye volume fraction of 0.82, in good agreement with the literature[22] (although 0.08 lower than XRR results). This suggests that the dye exhibits good TiO_2 surface passivation with respect to the solvent. Such protection of the TiO_2 surface can be attributed to the presence of hexyl alkyl chains on the thiophene moieties of **MK-2**.[56]

Using the same trigonometric considerations as per § 3.1.1, a tilt angle (α) of $56.6 \pm 7.1°$ was calculated. This means that the projection of a single molecule of **MK-2** onto the TiO_2 surface would theoretically occupy an area of 310.0 ± 58.9 Å^2, by multiplying molecular width with the molecular length as projected onto the TiO_2 surface ($L = d_{max}cos(\alpha)$). However, the measured APM, calculated using (**5**), was 64.6 ± 5.2 Å^2. This is five times smaller than the theoretical value of this area, suggesting that significant overlap of adjacent **MK-2** dye molecules must be present. **MK-2** dye molecules can overlap in two ways: facially, perpendicular to the plane of the molecular tilt, as described by the inter-dye spacing on the TiO_2 surface; or laterally, via the inter-digitation of hexa-alkyl chains on adjacent **MK-2** molecules (see Electronic Supplementary Information, §2.4). As per the XRR study, it is not possible to measure directly the extent of dye overlap. It is therefore more appropriate to

suggest a range of inter-dye separations. When **MK-2** is confined within a crystal lattice, five carbons on the hexa-alkyl chains overlap.[39] Assuming that this represents an upper boundary condition, lateral dye overlap could afford an effective dye molecular width that ranges anywhere from 9.79 Å (five-carbon overlap) to 19.89 Å (no overlap, **Figure 1**). Based on the observed APM value, the facial dye overlap (inter-dye spacing) could therefore range from 3.26-6.62 Å, which is in good accord with the XRR findings.

3.2.1.2 MK-2 dye⋯TiO₂ solid interface submerged within an electrolyte solution

Upon addition of lithium iodide, the **MK-2** dye-layer thickness remains constant within error. However, the SLD_n increases significantly to $2.5 \pm 0.1 \times 10^{-6}$ Å^{-2}, corresponding to a lower dye volume fraction of 0.65 and higher measured APM of 80.7 ± 6.5 Å^2. This indicates an increase in solvent ingress into the dye-layer, which could result from desorption of weakly bound or physisorbed species induced by solvent⋯dye or lithium⋯dye interactions,[37, 57-59] or an increase in the bulk solvent density (see Electronic Supplementary Information, §4).

NR measurements conducted after the formation of the I^-/I_3^- redox couple, induced by adding iodine to the lithium iodide (solution 3), are associated with a very modest change in SLD_n at best, corresponding to a dye volume fraction of 0.69 and measured APM of 81.4 ± 5.5 Å^2. Indeed, the SLD_n is the same as that of solution 2 within statistical error. This indicates that no further solvent ingress into the dye-layer occurs during the evolution of the redox couple from the lithium iodide reference point.

The origins of this dye SLD_n variation are presumably independent of the dye-layer thickness, given that there is no accompanying significant change in the dye-layer thickness observed upon addition of the electrolyte constituents. Such an elevation in dye SLD_n implies a significant increase in the mass density of the dye layer, given all other parameters in **Equation (4)** are constants for a given dye. A tighter packing of molecules could result from enhanced

ingress of solvent between the dye molecules; thus, an overall increase in the dye-layer SLD_n. The inclusion of I^- anions into the solution (with a large, positive coherent scattering length of 5.28 fm)[47] may also contribute to this increase in mass density. As such, this effect is deemed to originate primarily from the solvent phase, as opposed to a rearrangement of dye molecules on the surface; indeed, the latter scenario would likely be accompanied by a change in the dye-layer thickness which is not observed.

3.2.2 Buried MK-44 dye···TiO$_2$ solid interfaces

3.2.2.1 MK-44 dye···TiO$_2$ solid interface submerged within an acetonitrile solution

NR results indicate that the **MK-44** dye-layer is 9.2 ± 0.7 Å thick under a d$_3$-MeCN environment (solution 1). Given the Q range of the neutron reflectometry measurement, this parameter carries a noticeable standard deviation. However, the fitted value is in good agreement with the XRR determination, and the effective dye-layer contribution is substantial (see Figure S9 in the Electronic Supplementary Information, §3.1). The corresponding tilt angle of the dye with respect to the TiO$_2$ surface is 60.9 ± 7.9° while the calculated area per single molecule is 75.3 ± 18.3 Å^2, in good agreement with the values observed using XRR. The observed dye SLD_n is 2.9 ± 0.6 × 10^{-6} Å^{-2}, slightly larger than the calculated value (2.8 ×10^{-6} Å^{-2}; **Equation 2**). This could indicate that the dye layer may be experiencing some solvent ingress, with a dye volume fraction of 0.94 (**Equation 7**). It is worth noting here that the volume fraction observed here is much higher than observed using XRR (0.75), and it represents a near-complete dye coverage over the TiO$_2$ surface. This situation would imply a tight packing of dye molecules, which would manifest as shorter intermolecular distances. The APM of **MK-44** in solution 1 was determined to be 50.5 ± 3.9 Å^2 (**Equation 5**), which implies an inter-dye spacing of 3.4 ± 0.3 Å. Indeed, this is short, suggesting that the dyes are somewhat condensed together.

3.2.2.2 MK-44 dye⋯TiO$_2$ solid interface submerged within an electrolyte solution

The addition of lithium iodide to solution 1 (to create solution 2) results in a significant increase in dye-layer thickness, from 9.2 ± 0.7 Å to 15.9 ± 1.0 Å. The dye SLD$_n$ follows a similar trend, increasing from solution 1 to 2 but then remaining effectively constant between solutions 2 and 3. While the dye SLD$_n$ enhancement is bordering on statistical error assuming independent parameters, the dye layer and dye SLD$_n$ values follow the same trend between solutions 1-3 which suggests the changes have a correlated underlying structural origin. With this in mind, the increase in dye SLD$_n$ from solution 1 to 2 (**Table 3**) suggests a corresponding decrease in dye volume fraction to 0.57 (see **Equation 7**). As already intimated, further addition of I$_2$ (solution 3) sees all three parameters remaining relatively constant, with a dye thickness of 15.9 ± 1.0 Å and dye SLD$_n$ of $3.8 ± 0.4 × 10^{-6}$ Å^{-2} which corresponds to a slight reduction in dye volume fraction to 0.48 from solution 2.

This significant increase in dye-layer thickness realised upon the addition of the lithium iodide to the acetonitrile solution has important implications for the nature of the dye⋯TiO$_2$ anchoring mode. The XRR results provide evidence that **MK-44** anchors onto the TiO$_2$ surface via a bidentate binding configuration involving the cyanide and carboxylic acid groups of the cyanoacrylate moiety when the DSC working electrode is exposed to air (see §3.1.2.1). Based on the comparable dye-layer thickness obtained in these NR results of **MK-44** in solution 1, it would appear that this so-called CN/COO binding configuration is maintained when this dye⋯TiO$_2$ interface is immersed in acetonitrile solution. However, the much larger dye-layer thickness observed by NR for this interface in solutions 2 and 3 is inconsistent with this CN/COO binding configuration. Rather, it would seem that the addition of lithium iodide to the acetonitrile solution somehow causes a change in the **MK-44** dye⋯TiO$_2$ binding configuration such that the dye stands taller upon the TiO$_2$ surface, i.e. a thicker dye-layer results. One might anticipate that such a change could result in an associated modulation of the

dye SLD_n since the mass density of the dye layer may be affected; indeed, a 25% variation in this SLD_n is suggested by the NR data (see **Table 3**).

3.2.3 Influence of electrolyte constituents on the MK-44 dye binding configuration

A possible rationale behind these NR observations for **MK-44** could involve a mechanism whereby the lithium cations (Li^+) complex with the cyanide and carboxylate groups of the **MK-44** dye, in a manner illustrated in **Figure 6**. Indeed, Li^+ ions have been shown to strongly interact with both the carboxylate and cyanide moieties of cyanoacrylic groups bound to other dyes[57] on TiO_2 surfaces. In such an event, the ability of the **MK-44** dye to anchor onto the TiO_2 surface via the cyanoacrylic acid in the CN/COO binding configuration may be perturbed owing to competing interactions between the cyanoacrylic acid and the lithium cation. Accordingly, it might become more energetically favourable for the dye to adopt another type of binding configuration to circumvent this competition. To that end, the dye would presumably revert to the more common bidentate bridging dye$\cdots TiO_2$ binding configuration, as is observed in the **MK-2** dye (see §3.1.1.1).

UV/vis absorption spectroscopy was employed to experimentally check this hypothesis. Thereby, a red shift in the **MK-44** absorption spectrum was observed upon addition of lithium iodide to a film of **MK-44** sensitised TiO_2 (see Electronic Supplementary Information, §6, for further details). This bathochromic effect is indicative of the formation of dye$\cdots Li^+$ interactions[58], consistent with our hypothesis of **MK-44** dye$\cdots Li^+$ complexation, arising from our NR observations.
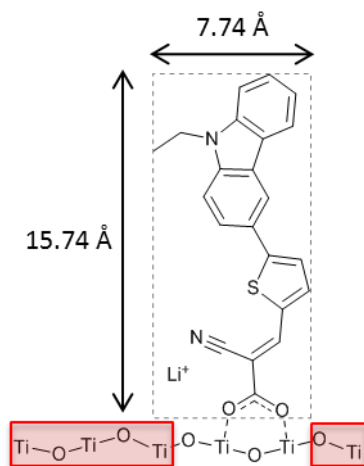
Figure 6 Molecular structure of **MK-44** with bidentate bridging geometry adopted in the presence of Li$^+$ ions, indicating the d_{max} (15.74 Å) and molecular width (7.74 Å). The red shaded boxes indicate sections of the TiO$_2$ surface which are potentially exposed to solvent/electrolyte upon the change in dye geometry.

Density functional theory (DFT) calculations were also employed in order to test this proposed mechanism. Accordingly, computational models of **MK-44** and the structure shown in **Figure 6** were generated and geometry optimised, in the absence and presence of Li$^+$ cations (see Electronic Supplementary Information, §7, for structural details). In the absence of Li$^+$ cations, the dye$\cdots$TiO$_2$ structure with a **MK-44** CN/COO binding mode was determined to be 0.19 eV lower in energy than that of the more common bidentate-bridging mode (as observed in **MK-2**). This is consistent with our *ex situ* XRR findings and the *in situ* NR structural results before Li$^+$ ions have been added to the solution environment. The reduction energy in this DFT comparison of adsorption modes is also consistent with the red shifting observed in the associated UV/vis absorption spectroscopy results mentioned above. Our DFT results are also corroborated by related computational work.[38]

The optimised geometry of the **MK-44** dye$\cdots$TiO$_2$ interfacial structure in the presence of Li$^+$ was then calculated, assuming that isomeric geometry is maintained upon addition of this

cation.[60] Li$^{+\cdots}$N and Li$^{+\cdots}$O interactions were both considered as possible binding options while **MK-44** was modelled according to two feasible adsorption modes, CN/COO and bidentate bridging. This afforded a total of six computational models of the dye$\cdots$TiO$_2$ interfacial structure in the presence of Li$^+$ ions. The lowest energy model featured a Li$\cdots$O interaction with a bidentate bridging adsorption mode. This stands to reason given that **MK-44** will manifest in a deprotonated state in acetonitrile solution such that Li$^+$ ions will be attracted to the negative charge on the carboxylate moiety.

These DFT results are also consistent with the NR measurements on the **MK-44** dye$\cdots$TiO$_2$ interface submerged under solution 2 or 3, where lithium ions are present, as manifested by a much thicker dye-layer (15.9 ± 1.0 Å in both cases), compared with that in solution 1 which is void of Li$^+$ ions, *c.f.* a **MK-44** dye-layer thickness of 9.2 Å. Indeed, a change in **MK-44** dye$\cdots$TiO$_2$ anchoring mode to a bidentate bridging geometry would result in a maximum observable layer thickness (d$_{BBmax}$) of 17.79 Å. This corresponds to the sum of the total length of the dye molecule, standing perpendicular to the TiO$_2$ surface in this bidentate bridging mode (15.74 Å), and the 2.05 Å dye$\cdots$TiO$_2$ separation (**Figure 6**). i.e. d$_{BBmax}$ corresponds well with those of NR results on the **MK-44** dye$\cdots$TiO$_2$ interface submerged under solutions 2 or 3.

The structural parameters that derive from this observed dye-layer thickness in solutions 2 and 3 also seem reasonable when considering a bidentate bridging dye$\cdots$TiO$_2$ anchoring mode: the tilt angle of the dye with respect to the TiO$_2$ surface is 63.3 ± 7.5°, and the theoretical APM is 61.8 ± 16.2 Å, as determined by the product of the **MK-44** molecular width (7.74 Å) and d$_{BBmax}$cos(α). This compares to the measured APM, as calculated using **Equation 5**, of 48.0 ± 3.0 Å and 57.1 ± 3.6 Å indicating approximately one **MK-44** molecule per measured area.

A further consequence of the surface rearrangement on this **MK-44** dye$\cdots$TiO$_2$ interface is that a greater proportion of the TiO$_2$ surface will likely become exposed to solvent. This can be

rationalised as follows. Since the dye sensitisation process is conducted prior to the addition of lithium iodide, the dye coverage is limited by the molecular footprint that the dye molecules initially cast on the TiO_2 as they bind in the CN/COO anchoring configuration. This molecular footprint is larger than that which would have been obtained if the dye had sensitised TiO_2 via the bidentate bridging mode where the dyes would have stood taller on the semiconductor surface. The initial binding of the dyes to TiO_2 in the CN/COO mode will have therefore effectively blocked binding sites on the TiO_2 surface that may have otherwise been accessible if the dyes had sensitised via a bidentate bridging anchoring mode. The large molecular footprint of the dye in the CN/COO binding configuration initially passivates the TiO_2 surface to solvent ingress. Yet, upon addition of lithium iodide, whereby the binding geometry changes to the bidentate bridging mode owing to dye$\cdots Li^+$ complexation, the previously blocked TiO_2 binding sites become exposed to solvent and thus electrolyte species. Since this occurs post-sensitisation, no additional dye molecules are available to occupy the vacancies created by this dye anchoring reconfiguration process. As such, this may have a detrimental effect on the photoelectrochemical performance of this dye in functioning DSC devices, as unwanted electron recombination reactions between the TiO_2 and electrolyte could readily occur.[21] Experimental evidence for this increased solvent ingress, as a function of dye$\cdots TiO_2$ binding reconfiguration, is indicated in the NR results via the slight increase in dye SLD_n value observed between solution 1 and solutions 2 and 3, i.e. upon the addition of lithium iodide.

4 Conclusions

This study has employed *ex situ* X-ray and *in situ* neutron reflectometry in order to determine structural characteristics of the **MK-2** and **MK-44** dye$\cdots TiO_2$ interfaces that relate to their function as DSC working electrodes. These characteristics comprise the average orientation of the dye with respect to the TiO_2 surface, the dye coverage of this surface, and average

intermolecular spacing between dye molecules once self assembled as a dye···TiO$_2$ interface. Both dyes self assemble onto the TiO$_2$ surface as monolayers, with dye coverage ranging from 75 to 90%. The dyes anchor onto the TiO$_2$ with tilt angles that subtend between 56.6 and 65.1°, depending on the sample environment. The hexa-alkyl chains that flank the sides of the **MK-2** dye appear to be inter-digitated, thereby forming a close-knitted dye-layer that passivates well the TiO$_2$ surface from unwanted electron recombination effects. In contrast, the inter-dye spacing of **MK-44** is sufficiently large that π···π interactions are ruled out.

These interfacial structures have been characterised within two sample environments: as exposed DSC working electrodes, and as working electrodes submerged under electrolyte solution that emulates the material conditions of the DSC functional device. The enabling of *in situ* neutron reflectometry to study these buried interfaces is particularly noteworthy since it represents the first time any materials characterisation method has probed the dye···TiO$_2$ interface within an electrolyte solution.

As such, the study reveals some significant new findings in terms of the function of lithium ions that form part of the electrolyte constituents. Specifically, these Li$^+$ ions are shown to complex with the **MK-44** dye, to the extent that the **MK-44** dye···TiO$_2$ anchoring mode changes from the CN/COO to bidentate bridging configuration upon addition of the electrolyte solution. This structural rearrangement of dyes exposes the TiO$_2$ surface to solvent and electrolyte attack which stands to deplete the photovoltaic performance of the corresponding DSC due to electron recombination effects.

Encouragingly, the results also show that the high-performance DSC dye, **MK-2**, does not undergo such a dye···TiO$_2$ binding reconfiguration upon addition of the electrolyte constituents. Rather, the **MK-2** dye is able to bestow the bidentate bridging mode from the process of dye sensitisation through to its functional device environment. The hexa-alkyl

groups which extrude from the **MK-2** dye, and are absent in **MK-44**, are presumably somewhat responsible for this stability in binding configuration. It is worth highlighting the specific role of the cyanoacrylate group in the salient results of this case study, and that this moiety has become probably the most popular anchoring group used for DSC dyes.[24] To this end, the structural trends observed in this study may well be found in many other classes of dyes and they therefore stand to have broader relevance to the DSC field.

Conflicts of Interest

There are no conflicts of interest to declare.

6 References

1.   O'Regan, B.; Gratzel, M., A low-cost, high-efficiency solar cell based on dye-sensitized colloidal TiO2 films. *Nature* **1991,** *353*, 737-740.

2.   Fakharuddin, A.; Jose, R.; Brown, T. M.; Fabregat-Santiago, F.; Bisquert, J., A perspective on the production of dye-sensitized solar modules. *Energy & Environmental Science* **2014,** *7* (12), 3952-3981.

3.   Xie, Z.; Jin, X.; Chen, G.; Xu, J.; Chen, D.; Shen, G., Integrated smart electrochromic windows for energy saving and storage applications. *Chemical Communications* **2014,** *50* (5), 608-610.

4.   Bechinger, C.; Ferrere, S.; Zaban, A.; Sprague, J.; Gregg, B. A., Photoelectrochromic windows and displays. *Nature* **1996,** *383* (6601), 608-610.

5.   Ahn, K.-S.; Yoo, S. J.; Kang, M.-S.; Lee, J.-W.; Sung, Y.-E., Tandem dye-sensitized solar cell-powered electrochromic devices for the photovoltaic-powered smart window. *Journal of Power Sources* **2007,** *168* (2), 533-536.

6.   Hagfeldt, A.; Grätzel, M., Molecular Photovoltaics. *Accounts of Chemical Research* **2000,** *33* (5), 269-277.

7.   Hagfeldt, A.; Boschloo, G.; Sun, L.; Kloo, L.; Pettersson, H., Dye-Sensitized Solar Cells. *Chemical Reviews* **2010,** *110* (11), 6595-6663.

8.   Ryan, M., PGM HIGHLIGHTS: Progress in Ruthenium Complexes for Dye Sensitised Solar Cells. *Platinum Metals Rev.* **2009,** *53* (4), 216.

9.   Qin, Y.; Peng, Q., Ruthenium Sensitizers and Their Applications in Dye-Sensitized Solar Cells. *International Journal of Photoenergy* **2012,** *2012*, 21.

10.   Ikeuchi, T.; Nomoto, H.; Masaki, N.; Griffith, M. J.; Mori, S.; Kimura, M., Molecular engineering of zinc phthalocyanine sensitizers for efficient dye-sensitized solar cells. *Chemical Communications* **2014,** *50* (16), 1941-1943.

11.   Mathew, S.; Yella, A.; Gao, P.; Humphry-Baker, R.; CurchodBasile, F. E.; Ashari-Astani, N.; Tavernelli, I.; Rothlisberger, U.; NazeeruddinMd, K.; Grätzel, M., Dye-sensitized solar cells with 13% efficiency achieved through the molecular engineering of porphyrin sensitizers. *Nat Chem* **2014,** *6* (3), 242-247.

12.   Yella, A.; Lee, H.; Tsao, H. N.; Yi, C.; Chandiran, A. K.; Nazeeruddin, M. K.; Diau, E. W.; Yeh, C.; Zakeeruddin, S. M.; Gratzel, M., Porphyrin-Sensitized Solar Cells with Cobalt (II/III)–Based Redox Electrolyte Exceed 12 Percent Efficiency. *Science* **2011,** *334 (6056)*, 629.

13.   Kakiage, K.; Aoyama, Y.; Yano, T.; Oya, K.; Fujisawa, J.-i.; Hanaya, M., Highly-efficient dye-sensitized solar cells with collaborative sensitization by silyl-anchor and carboxy-anchor dyes. *Chemical Communications* **2015,** *51* (88), 15894-15897.

14.   Wang, Z.-S.; Koumura, N.; Cui, Y.; Takahashi, M.; Sekiguchi, H.; Mori, A.; Kubo, T.; Furube, A.; Hara, K., Hexylthiophene-Functionalized Carbazole Dyes for Efficient Molecular Photovoltaics: Tuning of Solar-Cell Performance by Structural Modification. *Chemistry of Materials* **2008,** *20* (12), 3993-4003.

15.   El-Shafei, A.; Hussain, M.; Atiq, A.; Islam, A.; Han, L., A novel carbazole-based dye outperformed the benchmark dye N719 for high efficiency dye-sensitized solar cells (DSSCs). *Journal of Materials Chemistry* **2012,** *22* (45), 24048-24056.

16.   Alagumalai, A.; Fairoos, M.; Vellimalai, P.; Sil, M. C.; Nithyanandhan, J., Effect of Out-of-Plane Alkyl Group's Position in Dye-Sensitized Solar Cell Efficiency: A Structure–Property Relationship Utilizing Indoline-Based Unsymmetrical Squaraine Dyes. *ACS Appl. Mater. Interfaces* **2016**, 8, 35353-35367.

17.   Kroeze, J. E.; Hirata, N.; Koops, S.; Nazeeruddin, M. K.; Schmidt-Mende, L.; Grätzel, M.; Durrant, J. R., Alkyl chain barriers for kinetic optimization in dye-sensitized solar cells. *J. Am. Chem. Soc.* **2006**, 128, 16376-16383.

18.   Kay, A.; Grätzel, M., Artificial photosynthesis. 1. Photosensitization of titania solar cells with chlorophyll derivatives and related natural porphyrins. *J. Phys. Chem.* **1993**, 97, 6272-6277.

19.   He, J.; Benkö, G.; Korodi, F.; Polívka, T.; Lomoth, R.; Åkermark, B.; Sun, L.; Hagfeldt, A.; Sundström, V., Modified Phthalocyanines for Efficient Near-IR Sensitization of Nanostructured TiO2 Electrode. *J. Am. Chem. Soc.* **2002**, 124, 4922-4932.

20.   Katoh, R.; Furube, A., Electron injection efficiency in dye-sensitized solar cells. *Journal of Photochemistry and Photobiology C: Photochemistry Reviews* **2014,** *20* (0), 1-16.

21.   Gregg, B. A., Interfacial processes in the dye-sensitized solar cell. *Coordination Chemistry Reviews* **2004,** *248* (13–14), 1215-1224.

22.   Sewvandi, G. A.; Chen, C.; Ishii, T.; Kusunose, T.; Tanaka, Y.; Nakanishi, S.; Feng, Q., Interplay between Dye Coverage and Photovoltaic Performances of Dye-Sensitized Solar Cells Based on Organic Dyes. *The Journal of Physical Chemistry C* **2014,** *118* (35), 20184-20192.

23.   Krüger, J.; Bach, U.; Grätzel, M., Modification of TiO$_2$ Heterojunctions with Benzoic Acid Derivatives in Hybrid Molecular Solid-State Devices. *Advanced Materials* **2000,** *12* (6), 447-451.

24.   Zhang, L.; Cole, J. M., Anchoring Groups for Dye-Sensitized Solar Cells. *ACS Applied Materials & Interfaces* **2015,** *7* (6), 3427-3455.

25.   McCree-Grey, J.; Cole, J. M.; Evans, P. J., Preferred Molecular Orientation of Coumarin 343 on TiO$_2$ Surfaces: Application to Dye-Sensitized Solar Cells. *ACS Appl Mater Interfaces* **2015,** *7* (30), 16404-9.

26.   Griffith, M. J.; James, M.; Triani, G.; Wagner, P.; Wallace, G. G.; Officer, D. L., Determining the orientation and molecular packing of organic dyes on a TiO$_2$ surface using XRR. *Langmuir* **2011,** *27 (21)*, 12944-12950.

27.   Yu, S.; Ahmadi, S.; Zuleta, M.; Tian, H.; Schulte, K.; Pietzsch, A.; Hennies, F.; Weissenrieder, J.; Yang, X.; Göthelid, M., Adsorption geometry, molecular interaction, and charge transfer of triphenylamine-based dye on rutile TiO$_2$(110). *The Journal of Chemical Physics* **2010,** *133* (22), 224704.

28.   Brennan, T. P.; Tanskanen, J. T.; Bakke, J. R.; Nguyen, W. H.; Nordlund, D.; Toney, M. F.; McGehee, M. D.; Sellinger, A.; Bent, S. F., Dynamical Orientation of Large Molecules on Oxide Surfaces and its Implications for Dye-Sensitized Solar Cells. *Chemistry of Materials* **2013,** *25* (21), 4354-4363.

29.   Schiffmann, F.; VandeVondele, J.; Hutter, J.; Wirz, R.; Urakawa, A.; Baiker, A., Protonation-Dependent Binding of Ruthenium Bipyridyl Complexes to the Anatase(101) Surface. *The Journal of Physical Chemistry C* **2010,** *114* (18), 8398-8404.

30.   Voïtchovsky, K.; Ashari-Astani, N.; Tavernelli, I.; Tétreault, N.; Rothlisberger, U.; Stellacci, F.; Grätzel, M.; Harms, H. A., In Situ Mapping of the Molecular Arrangement of Amphiphilic Dye Molecules at the TiO$_2$ Surface of Dye-Sensitized Solar Cells. *ACS Applied Materials & Interfaces* **2015,** *7* (20), 10834-10842.

31.   Rienzo, A.; Mayor, L. C.; Magnano, G.; Satterley, C. J.; Ataman, E.; Schnadt, J.; Schulte, K.; O'Shea, J. N., X-ray absorption and photoemission spectroscopy of zinc protoporphyrin adsorbed on rutile TiO$_2$(110) prepared by in situ electrospray deposition. *The Journal of Chemical Physics* **2010,** *132* (8), 084703.

32.   Sasahara, A.; Pang, C. L.; Onishi, H., STM Observation of a Ruthenium Dye Adsorbed on a TiO$_2$(110) Surface. *The Journal of Physical Chemistry B* **2006,** *110* (10), 4751-4755.

33.   Kley, C. S.; Dette, C.; Rinke, G.; Patrick, C. E.; Čechal, J.; Jung, S. J.; Baur, M.; Dürr, M.; Rauschenbach, S.; Giustino, F.; Stepanow, S.; Kern, K., Atomic-Scale Observation of Multiconformational Binding and Energy Level Alignment of Ruthenium-Based Photosensitizers on TiO2 Anatase. *Nano Letters* **2014,** *14* (2), 563-569.

34.   Koumura, N.; Wang, Z.-S.; Mori, S.; Miyashita, M.; Suzuki, E.; Hara, K., Alkyl-Functionalized Organic Dyes for Efficient Molecular Photovoltaics. *Journal of the American Chemical Society* **2006,** *128* (44), 14256-14257.

35.   Hara, K.; Wang, Z.-S.; Cui, Y.; Furube, A.; Koumura, N., Long-term stability of organic-dye-sensitized solar cells based on an alkyl-functionalized carbazole dye. *Energy & Environmental Science* **2009,** *2* (10), 1109-1114.

36.   Suzuki, N.; Jiang, X.; Malgras, V.; Yamauchi, Y.; Islam, A.; Han, L., Synthesis of Thin Titania Photoanodes with Large Mesopores for Electricity-generating Windows. *Chemistry Letters* **2015,** *44* (5), 656-658.

37.   Koenigsmann, C.; Ripolles, T. S.; Brennan, B. J.; Negre, C. F. A.; Koepf, M.; Durrell, A. C.; Milot, R. L.; Torre, J. A.; Crabtree, R. H.; Batista, V. S.; Brudvig, G. W.; Bisquert, J.; Schmuttenmaer, C. A., Substitution of a hydroxamic acid anchor into the MK-2 dye for enhanced photovoltaic performance and water stability in a DSSC. *Physical Chemistry Chemical Physics* **2014,** *16* (31), 16629-16641.

38.   Zhang, F.; Ma, W.; Jiao, Y.; Wang, J.; Shan, X.; Li, H.; Lu, X.; Meng, S., Precise Identification and Manipulation of Adsorption Geometry of Donor–π–Acceptor Dye on Nanocrystalline TiO_2 Films for Improved Photovoltaics. *ACS Applied Materials & Interfaces* **2014,** *6* (24), 22359-22369.

39.   Cole, J. M.; Blood-Forsythe, M. A.; Lin, T-C.; Pattison, P.; Waddell, P. G.; Zhang, L.; Koumura, N.; Mori, S. *ACS Applied Materials & Interfaces*, accepted for publication.

40.   Churchill, M. R., Carbon-hydrogen and nitrogen-hydrogen distances assumed in, and determined from, recent x-ray diffraction studies on inorganic complexes. *Inorganic Chemistry* **1973,** *12* (5), 1213-1214.

41.   Martini, I.; Hodak, J. H.; Hartland, G. V., Effect of Structure on Electron Transfer Reactions between Anthracene Dyes and TiO_2 Nanoparticles *J. Phys. Chem. B* **1998**, *102*, 9508-9517.

42.   Manzhos, S.; Giorgi, G.; Yamashita, K., A Density Functional Tight Binding Study of Acetic Acid Adsorption on Crystalline and Amorphous Surfaces of Titania, *Molecules* **2015**, *20*, 3371-3388.

43.   Triani, G.; Campbell, J. A.; Evans, P. J.; Davis, J.; Latella, B. A.; Burford, R. P., Low temperature atomic layer deposition of titania thin films. *Thin Solid Films* **2010,** *518* (12), 3182-3189.

44.   Nelson, A., Co-refinement of multiple-contrast neutron/X-ray reflectivity data using MOTOFIT. *Journal of Applied Crystallography* **2006,** *39* (2), 273-276.

45.   James, M.; Nelson, A.; Holt, S. A.; Saerbeck, T.; Hamilton, W. A.; Klose, F., The multipurpose time-of-flight neutron reflectometer "Platypus" at Australia's OPAL reactor. *Nuclear Instruments and Methods in Physics Research Section A: Accelerators, Spectrometers, Detectors and Associated Equipment* **2011,** *632* (1), 112-123.

46.   Heinrich, F.; Ng, T.; Vanderah, D. J.; Shekhar, P.; Mihailescu, M.; Nanda, H.; Lösche, M., A New Lipid Anchor for Sparsely Tethered Bilayer Lipid Membranes. *Langmuir* **2009,** *25* (7), 4219-4229.

47.   Sears, V. F., Neutron Scattering Lengths and Cross Sections *Neutron News* **1992,** *3* (3), 26-37.

48.   Triani, G.; Evans, P. J.; Mitchell, D. R. G.; Attard, D. J.; Finnie, K. S.; James, M.; Hanley, T.; Latella, B.; Prince, K. E.; Bartlett, J. Atomic layer deposition of TiO_2 / Al_2O_3 films for optical applications. In *Proc. SPIE 5870, Advances in Thin Film Coatings for Optical Applications II*, **2005**, 587009/1 - 587009/10.

49.   Frisch, M. J.; Trucks, G. W.; Schlegel, H. B.; Scuseria, G. E.; Robb, M. A.; Cheeseman, J. R.; Scalmani, G.; Barone, V.; Mennucci, B.; Petersson, G. A.; Nakatsuji, H.; Caricato, M.; Li, X.; Hratchian, H. P.; Izmaylov, A. F.; Bloino, J.; Zheng, G.; Sonnenberg, J. L.; Hada, M.; Ehara, M.; Toyota, K.; Fukuda, R.; Hasegawa, J.; Ishida, M.; Nakajima, T.; Honda, Y.; Kitao, O.; Nakai, H.; Vreven, T.; Montgomery, J., J. A.; ; Peralta, J. E.; Ogliaro, F.; Bearpark, M.; Heyd, J. J.; Brothers, E.; Kudin, K. N.; Staroverov, V. N.; Kobayashi, R.; Normand, J.; Raghavachari, K.; Rendell, A.; Burant, J. C.; Iyengar, S. S.; Tomasi, J.; Cossi, M.; Rega, N.; Millam, J. M.; Klene, M.; Knox, J. E.; Cross, J. B.; Bakken, V.; Adamo, C.; Jaramillo, J.; Gomperts, R.; Stratmann, R. E.; Yazyev, O.; Austin, A. J.; Cammi, R.; Pomelli, C.; Ochterski, J. W.; Martin, R. L.; Morokuma, K.; Zakrzewski, V. G.; Voth, G. A.; Salvador, P.; Dannenberg, J. J.; Dapprich, S.; Daniels, A. D.; Farkas, Ö.; Foresman, J. B.; Ortiz, J. V.; Cioslowski, J.; Fox, D. J. *Gaussian Inc.*, Wallingford CT, **2009**.

50.   Sanchez-de-Armas, R.; San Miguel, M. A.; Oviedo, J.; Sanz, J. F., Coumarin derivatives for dye sensitized solar cells: a TD-DFT study. *Physical Chemistry Chemical Physics* **2012,** *14* (1), 225-233.

51.   Sánchez-de-Armas, R.; Oviedo López, J.; A. San-Miguel, M.; Sanz, J. F.; Ordejón, P.; Pruneda, M., Real-Time TD-DFT Simulations in Dye Sensitized Solar Cells: The Electronic Absorption Spectrum of Alizarin Supported on TiO_2 Nanoclusters. *Journal of Chemical Theory and Computation* **2010,** *6* (9), 2856-2865.

52.   Becke, A. D., Density-functional thermochemistry. III. The role of exact exchange. *The Journal of Chemical Physics* **1993,** *98* (7), 5648-5652.

53.   Harms, H. A.; Tetreault, N.; Gusak, V.; Kasemo, B.; Gratzel, M., In situ investigation of dye adsorption on TiO_2 films using a quartz crystal microbalance with a dissipation technique. *Physical Chemistry Chemical Physics* **2012,** *14* (25), 9037-9040.

54.   Nepomnyashchii, A. B.; Parkinson, B. A., Influence of the Aggregation of a Carbazole Thiophene Cyanoacrylate Sensitizer on Sensitized Photocurrents on ZnO Single Crystals. *Langmuir* **2013,** *29* (30), 9362-9368.

55.   Janiak, C., A critical account on $\pi-\pi$ stacking in metal complexes with aromatic nitrogen-containing ligands. *Journal of the Chemical Society, Dalton Transactions* **2000,** (21), 3885-3896.

56.   Koumura, N.; Wang, Z.-S.; Miyashita, M.; Uemura, Y.; Sekiguchi, H.; Cui, Y.; Mori, A.; Mori, S.; Hara, K., Substituted carbazole dyes for efficient molecular photovoltaics: long electron lifetime and high open circuit voltage performance. *Journal of Materials Chemistry* **2009,** *19* (27), 4829-4836.

57.   Basu, J. K.; Shannigrahi, M.; Bagchi, S., Lithium Ion–Ketocyanine Dye Interactions in the Ground and Excited States. *The Journal of Physical Chemistry A* **2006,** *110* (29), 9051-9056.

58.   Furube, A.; Katoh, R.; Hara, K.; Sato, T.; Murata, S.; Arakawa, H.; Tachiya, M., Lithium Ion Effect on Electron Injection from a Photoexcited Coumarin Derivative into a TiO_2 Nanocrystalline Film Investigated by Visible-to-IR Ultrafast Spectroscopy. *The Journal of Physical Chemistry B* **2005,** *109* (34), 16406-16414.

59.   Heo, N.; Jun, Y.; Park, J. H., Dye molecules in electrolytes: new approach for suppression of dye-desorption in dye-sensitized solar cells. *Sci. Rep.* **2013,** *3(1712),* 1-6.

60.   Balanay, M. P.; Kim, S.-M.; Lee, M. J.; Lee, S. H.; Kim, D. H., Conformational Analysis and Electronic Properties of 2-Cyano-3-(thiophen-2-yl)acrylic Acid in Sensitizers for Dye-sensitized Solar Cells: A Theoretical Study. *Bulletin of the Korean Chemical Society* **2009,** *30* (9), 2077-2082.

Table of Contents Graphic